buildings

MDPI

Article

Experimental Investigation on Mechanical Bearing Characteristics and Crack Evolution Mechanism of Coal Pillar "Excavation-Backfill" Composites

Haiqing Shuang [1,2], Jingmin Zhang [1,*], Xuhui Ma [1] and Jin Zhang [3,*]

[1] School of Safety Science and Engineering, Xi'an University of Science and Technology, Xi'an 710054, China
[2] Key Laboratory of Western Mines and Hazards Prevention, Ministry of Education of China, Xi'an 710054, China
[3] College of Environmental and Chemical Engineering, Xi'an Polytechnic University, Xi'an 710600, China
* Correspondence: zhang_jm@stu.xust.edu.cn (J.Z.); zhangjin@xpu.edu.cn (J.Z.)

Abstract

To investigate the mechanical bearing characteristics of the "excavation-backfill" composite after the excavation of coal pillars and backfill replacement with gangue-based cemented paste backfill, mechanical bearing characteristic experiments are conducted on a series of coal samples with rectangular "excavation-backfill" roadways under uniaxial loading, covering the full deformation and failure process. The MTS universal testing machine and DS5-type acoustic emission signal acquisition system are employed, and a high-speed camera is adopted to monitor and record the full failure process. The mechanical bearing characteristics and crack evolution mechanisms of unfilled coal pillar (U-C) and backfill coal pillar (B-C) samples are explored. The results show that with the increase in "excavation-backfill" width, the uniaxial compressive strength and elastic modulus of U-C samples decrease significantly, and the samples exhibit brittle–ductile failure. When the "excavation-backfill" width is 60 mm, the backfill can distinctly improve the strength and elastic modulus of B-C samples, showing a strong strength recovery effect. The temporal characteristics of AE signals indicate that both U-C and B-C samples experience four stages subjected to uniaxial compression: quiet period, rising period, active period, and post-peak rising period. In the quiet period and rising period, the *b*-value fluctuates upward with energy release; in the active period, the *b*-value decreases significantly with large energy release; in the post-peak rising period, crack propagation and frictional slip increase, leading to an enlarged fluctuation amplitude of the *b*-value. Based on the location of AE sources, the three-dimensional crack chain evolution is inverted. The crack chain evolution of the U-C is mainly distributed along the dip direction (75°~90°, 255°~270°) and vertical direction (165°~180°) of the coal bedding plane, while the B-C is more uniform, indicating that the backfill evidently affects the crack distribution. This study provides new insights for predicting the crack evolution and failure mode of coal–rock composites.

Keywords: coal pillar "excavation-backfill" composites; acoustic emission; compressive strength; 3D crack chain evolution

Check for updates

Academic Editor: Salvatore Verre

Received: 6 February 2026
Revised: 26 February 2026
Accepted: 3 March 2026
Published: 6 March 2026

Copyright: © 2026 by the authors. Licensee MDPI, Basel, Switzerland. This article is an open access article distributed under the terms and conditions of the Creative Commons Attribution (CC BY) license.

1. Introduction

In China, constrained by conditions such as coal seam thickness and burial depth, roadway support faces significant challenges. The practice of leaving coal pillars is commonly

adopted to ensure the safety of working face roadways, with the width of reserved coal pillars mostly exceeding 20 m, which causes a significant waste of coal resources. Against this backdrop, Wang et al. [1] proposed the integrated "excavation-backfill-retention" mining technology for inter-panel coal pillars. On one hand, it aims to recover coal resources before the influence of mining activities; on the other hand, the excavation width of large-section roadways and the backfill width of the central zone are calculated based on the mine gangue output, realizing the disposal of mine excavation gangue in the central backfill zone. After the "excavation-backfill" of coal pillars, the backfill and the hollow rectangular structure form an "excavation-backfill" composite that jointly bears the overlying load. The mechanical bearing characteristics and failure mechanism of the composite are the core issues determining its stable load-bearing capacity.

Currently, numerical simulation and similar material simulation are the main methods for studying the bearing characteristics and failure mechanism of roadway surrounding rock structures. For instance, Wang et al. [2] used FLAC^{3D} to investigate the surrounding rock instability response mechanism of gob-side entry retaining during section coal pillar recovery. Qiao et al. [3] studied the failure mechanism of coal pillars and surrounding rock control technology under the influence of secondary mining through numerical simulation. Xie et al. [4] employed 3DEC to simulate the excavation process of layered fractured rock mass of Jinchuan No.2 Mine, revealing the mechanical characteristics and fracture evolution law of surrounding rock during the excavation of deep-buried fractured rock mass roadways. Sayadi et al. [5] carried out a set of unconfined compression tests on prismatic granite specimens with a central circular hole and paired prefabricated flaws at various inclination angles, and further identified and distinguished the different cracking stages of the specimens during the whole process prior to ultimate failure. Wang et al. [6] explored the progressive deterioration characteristics of granite under cyclic thermal shock loading, and the results indicated that the rock presented a brittle-to-ductile transition behavior, which was accompanied by a notable enhancement in acoustic emission activity. Jing et al. [7] conducted large-scale physical model tests on the entire bearing process of roadway surrounding rock under different support strengths, investigating the full process of deformation and fracture evolution of roadway surrounding rock through multi-source information responses of force, electricity, magnetism, and AE. These studies have explored the bearing characteristics and failure mechanism of roadway surrounding rock structures from various perspectives through numerical simulation and similar material simulation, providing effective means for hazard prediction.

However, to more accurately reveal the failure process and mechanical response of roadway surrounding rock under actual stress conditions, physical model tests have gradually become an important research direction. In an infinite stratum, the existence of roadway can be analogous to a hole or cavity in underground rock formations. Therefore, studying the failure and crack evolution laws of rocks containing holes and cavities can effectively reflect the failure laws of roadway surrounding rock [8–10]. For example, Chang et al. [11] carried out true triaxial tests on limestone samples with circular holes to explore the spalling-rock burst failure mechanism of roadway surrounding rock in high-stress environments. Xin et al. [12,13] conducted physical shear failure tests on hard rock caverns using red sandstone samples, considering four key controlling factors affecting the shear failure behavior of caverns (i.e., cavern number, cross-sectional shape, cavern spacing, and backfill), and revealed the deformation law, failure mode, and instability mechanism of cavern surrounding rock under strong shear. Zhu et al. [14] performed coupled static–dynamic loading tests on diorite specimens under three different filling states (unfilled, single-filled, and double-filled), investigating the influence of filling on the mechanical response and fracture behavior of pre-stressed rock with double rectangular holes under

dynamic loads. Lee et al. [15] studied the acoustic emission response characteristics during the formation of damaged zones around circular openings, and found that tensile failure occurred along the direction parallel to the maximum compressive stress axis with the increase in applied load. Zhu et al. [16] conducted uniaxial compression tests on plate-shaped marble specimens with prefabricated elliptical holes, exploring the influence of the aspect ratio and inclination angle of the ellipse on the mechanical properties of marble, and recorded and analyzed the deformation and fracture process of the specimens using digital image correlation (DIC) technology. Liu et al. [17] studied the deformation and failure characteristics and acoustic properties of sandstone with different roadway shapes under cyclic loading and unloading. Wu et al. [18] investigated the mechanical properties and fracture characteristics of red sandstone specimens with five hole shapes under uniaxial loading. Gong et al. [19] studied the spalling process of deep-buried rectangular tunnel excavation under triaxial stress, performed physical simulation tests of rectangular tunnels using a true triaxial test system, and recorded and monitored in real-time the damage process of the rectangular tunnel sidewalls with a high-speed camera. Wu et al. [20] systematically studied the influence of hole shape on the mechanical properties and fracture characteristics of rocks under uniaxial compression, finding that the presence of holes significantly impairs the mechanical properties of rocks. Zhou et al. [21] conducted uniaxial compression tests on specimens with single and double rectangular holes, revealing that the mechanical properties of specimens with double rectangular holes deteriorate more severely than those with a single rectangular hole. Despite numerous studies focusing on the failure mechanism and mechanical response of surrounding rock structures with holes and cavities, research on the mechanical bearing characteristics and failure laws of composites composed of coal pillars with rectangular roadways and backfill is relatively scarce.

To reveal the mechanical bearing characteristics and crack evolution mechanism of coal pillars after excavation and backfill, unfilled coal pillar (U-C) and backfill coal pillar (B-C) coal samples are prepared. This study innovatively combines AE multi-parameter analysis (*b*-value, RA-AF), DIC full-field strain measurement, and machine learning-based SLC clustering to invert the 3D crack chain evolution, and quantifies the strength recovery effect of gangue-based cemented paste backfill with different excavation–backfill widths. It also clarifies the regulatory mechanism of backfill on the crack distribution and failure mode of coal pillar composites, providing a novel experimental and methodological basis for the engineering application of coal pillar "excavation-backfill-retention" mining technology.

2. Experimental Design

2.1. Experimental Materials and Protocol

After cutting, grinding, and drilling, unfilled coal pillar (U-C) and backfill coal pillar (B-C) specimens are cast with backfill in the laboratory, as illustrated in Figure 1. The gangue-based cemented paste backfill has an optimized mass ratio of cement: fly ash: gangue powder: water = 1:1:3:1.83 [10,22]. Specifically, the gangue powder is obtained from the gangue after secondary screening and crushing in a coal preparation plant, and the water used is laboratory tap water. The mechanical parameters of the materials are presented in Table 1. All specimens are subjected to standard curing in a constant temperature and humidity chamber for 28 days (relative humidity: 95% $\pm$ 1%, temperature: 20 $\pm$ 1 °C).

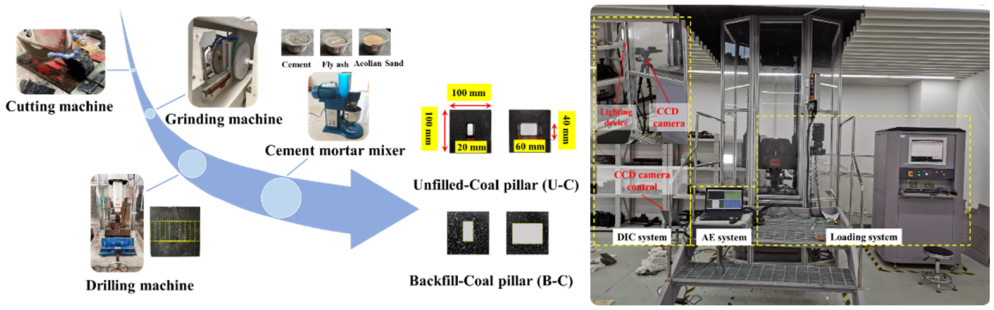

(**a**) Specimen processing flow chart (**b**) Experimental schematic diagram

Figure 1. Specimen preparation and test methods.

Table 1. Mechanical parameters of material.

Items	Compressive Strength/MPa	Tensile Strength/MPa	Shear Strength/MPa
Coal	22.95	0.47	12.63
backfill	6.70	0.81	3.93

To investigate the failure characteristics of U-C and B-C composites under different "excavation-backfill" widths, two sets of cubic specimens (100 × 100 × 100 mm) are fabricated, with precast rectangular roadways of dimensions 20 × 40 mm and 60 × 40 mm, respectively. One group is filled corresponding to the precast rectangular roadways, and each group of three specimens is tested. The experimental protocol is summarized in Table 2.

Table 2. Experimental protocol.

Items	Excavation–Backfill Width/mm	Excavation–Backfill Height/mm
U-C	0/20/60	40
B-C	20/60	40

2.2. Experimental Equipment and Setup

As shown in Figure 1b, the testing system consists of three subsystems: a uniaxial loading system, an acoustic emission (AE) monitoring system, and a digital image correlation (DIC) processing and imaging system. These systems operate simultaneously to synchronously collect data, ensuring accurate correlation between the mechanical behavior, AE responses, and surface deformation field. The detailed information and corresponding settings of each testing instrument are introduced in detail below.

The uniaxial compression tests are conducted using an Instron1346 servo-hydraulic universal testing machine. To eliminate the frictional effect on the loading surfaces, lubricating oil is applied to the loading plates before testing. During the tests, the lower rigid loading plate moves upward under displacement control at a loading rate of 1 mm/min, while the upper rigid loading plate remains stationary.

To detect the internal crack evolution characteristics of the specimens, six AE sensors with a 40 dB noise threshold are fixed at the center of the front and back face of the cubic specimens (100 × 100 × 100 mm), with vaseline as the coupling agent to ensure tight acoustic contact between the sensors and the specimen surface, eliminating signal transmission loss.

The specimen surface is first polished and cleaned to remove dust and unevenness, then a matte white primer is uniformly sprayed as the background, followed by manual dotting of random black matte speckles (2–3 pixels in diameter, 3–4 pixels in

spacing) to ensure uniform, non-agglomerated speckles. DIC parameters are specified as 2448 × 2050 pixel camera resolution, 8-bit grayscale digitization, 10 fps sampling frequency, and 0.0588 mm/pixel scale ratio, with the MatchID-2D/Stereo system for capture and GOM software for analysis.

3. Experimental Results and Analysis

3.1. Mechanical Behavior

3.1.1. Stress–Strain Curve Characteristics

Stress–strain curves can effectively reflect the mechanical response of U-C and B-C specimens subjected to uniaxial compression. Figure 2 presents the stress–strain relationships of the two groups of specimens (U-C and B-C); both U-C and B-C specimens exhibit four typical stages: pore compaction stage, elastic stage, yield stage, and post-peak residual stage. Notably, compared with the U-C group, the B-C group has an evident post-peak residual stage.

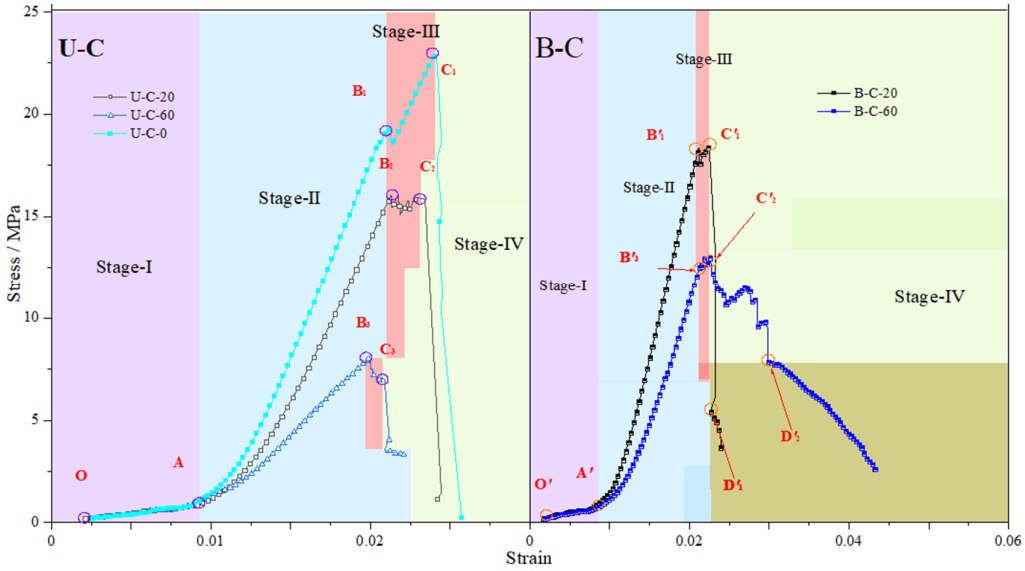

Figure 2. Stress and strain curves of U-C and B-C specimens.

In the pore compaction stage, due to the structural effect of the U-C group, the strain values are distributed between 0.008 and 0.01. The strain of both U-C and B-C specimens is mainly affected by the pores and fractures in the coal. In the elastic stage, the elastic modulus of the specimens decreases with the increase in excavation–backfill width, and the rate of internal energy accumulation slows down. In the yield stage, micro-cracks rapidly propagate and coalesce to form macro-cracks, and the specimens enter an unstable failure; the energy of acoustic emission (AE) events surges, and both U-C and B-C specimens exhibit certain ductile failure characteristics [23], with local instability of some specimens leading to pre-peak stress drops. In the post-peak residual stage, as the excavation–backfill width increases, the U-C group changes from one post-peak stress drop to two. This is because the failure mode of the U-C group transforms from tensile failure of the roadway roof to tensile–shear failure of the roof and coal wall. Unlike the U-C group, the post-peak stress of the B-C group drops to approximately 5~7 MPa, and the specimens enter the post-peak residual stage, where the load-bearing effect is mainly governed by the backfill.

3.1.2. Mechanical Parameters

Based on the stress–strain curves, the influence of excavation–backfill width on the mechanical parameters of U-C and B-C specimens is further summarized. As shown in

Table 3, the uniaxial compressive strength and elastic modulus of U-C-0 (i.e., intact coal sample) are 22.95 MPa and 14.62 GPa, respectively. For the U-C, when the excavation–backfill width increases from 0 mm to 20 mm and then to 60 mm, the uniaxial compressive strength of the specimens continuously decreases from 22.95 MPa to 8.06 MPa, with a decrease of 30.07% and 64.88% respectively, showing an increasing trend of strength degradation. A similar trend is observed for the elastic modulus. This is because the specimens are subjected to uniform force without large local defects, and the loading process is only affected by the size of the rectangular excavated roadway. For the B-C, when the excavation–backfill width increases from 20 mm to 60 mm, the uniaxial compressive strength of the specimens decreases from 18.40 MPa to 13.0 MPa, with a decrease of 19.83 and 43.36%, but it is higher than that of the corresponding U-C. This is because the main load-bearing of the specimen shifts from coal-dominated bearing to the combined bearing of coal and backfill, which is evidenced by the peak strain difference ε_{60} (U-C-60, B-C-60) of 0.0201 and 0.0226, respectively.

Table 3. Uniaxial compression test results of U-C and B-C specimens.

Items	Compressive Strength/MPa	Elastic Modulus/GPa	Peak Strain (ε)	R (%)
U-C-0	22.95 ± 0.052	14.62 ± 0.33	0.0241 ± 0.0009	-
U-C-20	16.05 ± 0.47	12.63 ± 0.28	0.0228 ± 0.0007	30.07
U-C-60	8.06 ± 0.32	6.37 ± 0.21	0.0201 ± 0.0006	64.88
B-C-20	18.40 ± 0.51	13.79 ± 0.30	0.0212 ± 0.0007	19.83
B-C-60	13.0 ± 0.45	9.43 ± 0.25	0.0226 ± 0.0007	43.36

Note: Strength reduction rate $R = (\sigma_0 - \sigma)/\sigma_0 \times 100\%$ (σ_0 for U-C-0 strength).

3.2. Acoustic Emission Characteristics

3.2.1. Analysis of AE Ringing Counts

Figure 3 presents the real-time curves of stress, AE ringing counts, and cumulative AE ringing counts during the full compressive deformation and failure process of U-C and B-C specimens under different excavation–backfill widths. Based on the temporal characteristics of AE signals in Figure 3, both the U-C and B-C groups exhibit a four-stage AE evolution law during uniaxial compression: quiet period, rising period, active period, and post-peak rising period. The post-peak rising period is mainly observed in the B-C group.

Quiet period: This stage corresponds to the compaction stage of the stress–strain curve, with the stress at the end of the stage being approximately 1.0 MPa. The existing micro-fractures of the specimens are compacted, but their activity amplitude does not exceed the AE threshold, resulting in low-level fluctuations overall and steady growth of the ringing count curve.

Rising period: This stage corresponds to the elastic stage and part of the yield stage. The maximum load-bearing capacity of most specimens reaches approximately 90% of the compressive strength, such as U-C-0, U-C-20, B-C-20, and B-C-60. During this stage, internal cracks of the specimens develop stably, and micro-cracks gradually expand to form macrocracks at the end of the stage, leading to plastic damage failure of the specimens. This causes occasional large-scale AE events, resulting in local abrupt increases in AE ringing counts. The AE ringing counts are active during the rising period, and the cumulative ringing count shows an obvious growth trend.

Active period: When the stress exceeds 90% of the compressive strength, the evolution of internal cracks in the specimens intensifies, and a large number of cracks coalesce to form macrocracks. The specimens undergo unstable failure to varying degrees, with a sharp increase in AE events and a dramatic rise in the cumulative ringing count.

Post-peak rising period: This stage is mainly reflected in the loading process of B-C specimens. The incorporation of the backfill significantly alters the post-peak mechanical behavior of U-C samples. With the increase in excavation–backfill width, the proportion of post-peak rising time increases markedly. During this stage, the AE count increases relatively slowly, and the AE signals are dominated by low-energy frictional events, reflecting the frictional slip behavior between fracture interfaces.

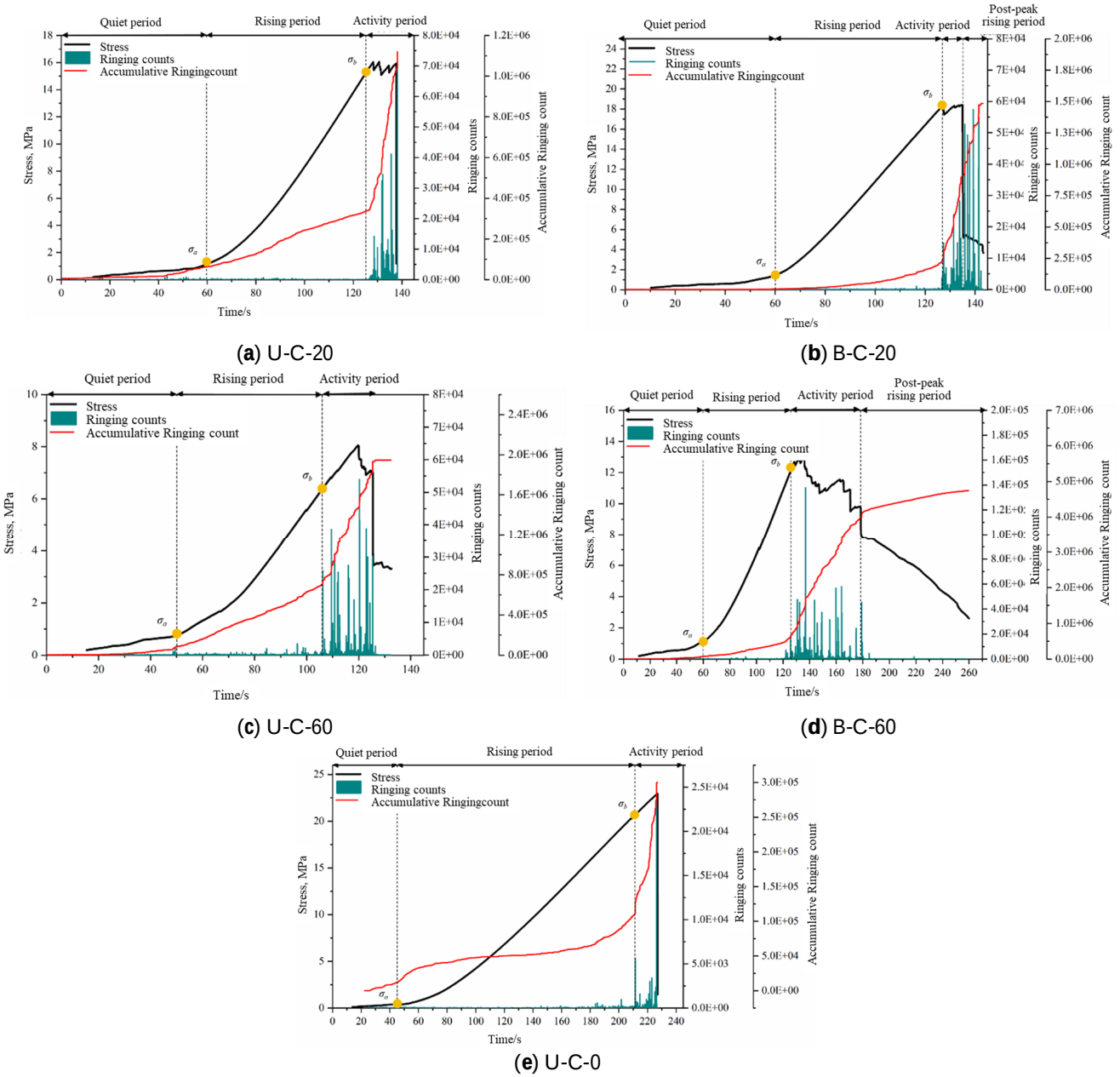

Figure 3. Stress, AE counts, and cumulative AE counts vs. time of U-C and B-C specimens.

Due to the influence of excavation–backfill width, the laws of the specimens show certain differences, attributed to the transformation of the failure mode. For the U-C group, in the rising period, when the specimen is an intact coal sample (U-C-0), the AE event rate is low, the AE count is stable, and the growth rate of the cumulative count is at a low level. Macroscopically, tensile cracks occur along the weak bedding planes of the U-C, and the coal wall undergoes flaky spalling. When the excavation–backfill width is 20 mm, the specimen generates both tensile cracks along the weak bedding planes and shear cracks

due to transverse deformation during loading, with higher AE counts and event rates. When the excavation–backfill width is 60 mm, the specimen is mainly characterized by transverse shear cracks, with fewer cracks generated and lower AE counts and event rates. Detailed analysis is provided in Section 4.2. For the B-C group, the AE counts and events are relatively few during the rising period, and the cumulative AE count increases steadily. In the active period, when the excavation–backfill width is 20 mm, the transverse deformation reaches the tensile limit of the specimen, leading to rapid development and crack coalescence. When the excavation–backfill width is 60 mm, the specimen slides along the shear failure interface, resulting in a sudden increase in AE counts.

3.2.2. Analysis of b-Value

As a key scaling parameter, the *b*-value is widely used to characterize the stress state and medium properties, calibrating the scaling relationship between the number and size of material micro-fractures and reflecting the degree of fracture propagation [24–26]. The AE is related to the energy release mode of seismic activities, but it differs from the seismic magnitude-based calculation system in seismology. Gutenberg [27] proposed the relationship between seismic frequency and magnitude (Equation (1)), revealing the essential characteristics of tectonic stress accumulation and release:

$$\lg N = a - bM \tag{1}$$

where M is the seismic magnitude, N is the seismic frequency, and a and b are constants.

When calculating the *b*-value, the AE amplitude (A) is usually divided by the sensor sensitivity calibration parameter (20) instead of the seismic magnitude (Equation (2)):

$$M_A = A/20 \tag{2}$$

where A represents the AE amplitude, M_A denotes the AE magnitude, and the coefficient 20 is derived from the sensor sensitivity calibration parameter.

In this study, the reference sampling window is set to 100 AE events, consistent with Zhang et al. [25], who demonstrated that this window balances temporal resolution and stability—avoiding excessive fluctuations from smaller windows or delayed response from larger ones. To reduce the interference of noise data from previous and subsequent samples on the *b*-value results, the sliding window is set to 10 AE events, and an overlap rate of 90% between sampling windows is adopted to improve the temporal resolution of the *b*-value [26]. Considering the correlation between the *b*-value and energy, the comparison between AE energy and *b*-value characteristics is plotted in Figure 4.

As shown in Figure 4, in compaction and elastic stages of U-C and B-C specimens, the internal damage is mainly the closure and propagation of small-scale initial fractures and new fractures. The evolution of numerous fractures is accompanied by the release of minor elastic energy, resulting in fluctuating upward *b*-values and fluctuations in AE energy. In the yield stage, the *b*-value of the specimens decreases significantly, which is because small-scale fractures gradually coalesce to form large-scale fractures, and the energy storage of large-scale fractures further coalesces into macrocracks, with the energy storage being reflected by the substantial energy. In the post-peak residual stage, the number of frictional, dislocation slip, and cracking in the macro-fracture zone increases with the increase in excavation–backfill width, releasing more elastic energy, leading to a larger fluctuation amplitude of the *b*-value and fluctuations in the energy curve.

Notably, the *b*-value curve of B-C-60 fluctuates more violently compared to other specimens; the specimens exhibit certain load-bearing characteristics both at the yield stage and post-peak residual stage. This is due to the role of the backfill in the composite

structure, since the backfill contains a large number of porous structures and its load-bearing behavior is mostly characterized by shear failure. Under loading, internal aggregate friction, cementitious material cracking, and closure of primary pores lead to a gradual increase in the scale of small-scale micro-fractures inside the specimens. Due to the stress-bearing characteristics of the backfill, micro-cracks continue to evolve and form in the post-peak residual stage, resulting in continuous fluctuations of the *b*-value.

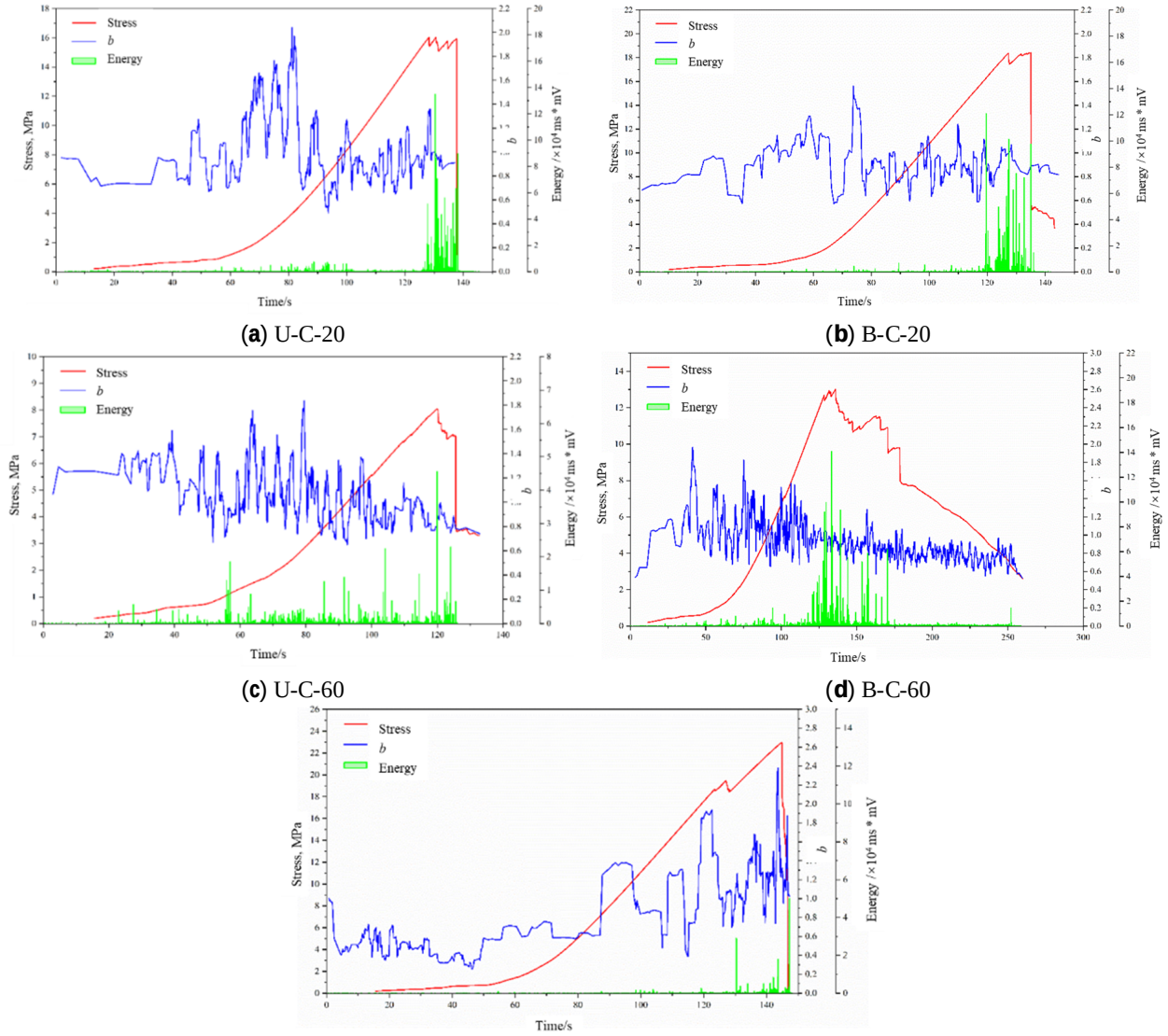

(**a**) U-C-20 (**b**) B-C-20

(**c**) U-C-60 (**d**) B-C-60

(**e**) U-C-0

Figure 4. The relationship between stress, *b*-value, and energy vs. time of U-C and B-C specimens.

3.2.3. Analysis of RA-AF Characteristic

RA and AF are commonly used AE parameter methods for distinguishing failure types. The RA value is defined as the rise time divided by the signal amplitude (ms/V), and AF is defined as the AE ringing count divided by the signal duration (kHz). The combination of RA and AF values of AE signals is used to distinguish failure types: tensile failure is characterized by a higher AF value and a lower RA value, while shear failure is associated with a lower AF value and a higher RA value. Based on the calculation and crack classification method proposed by Liu et al. [28], and using K-means clustering analysis, we identified the optimal threshold (RA = 0.8 ms/V, AF = 8 kHz) by minimizing the intra-cluster variance of tensile and shear crack signals—this calibration accounted for

the backfill's porous structure and coal's bedding characteristics, which differ from rock. the AE parameters of the U-C and B-C groups are calculated to obtain RA and AF values, and high-density scatter plots are drawn as shown in Figure 5.

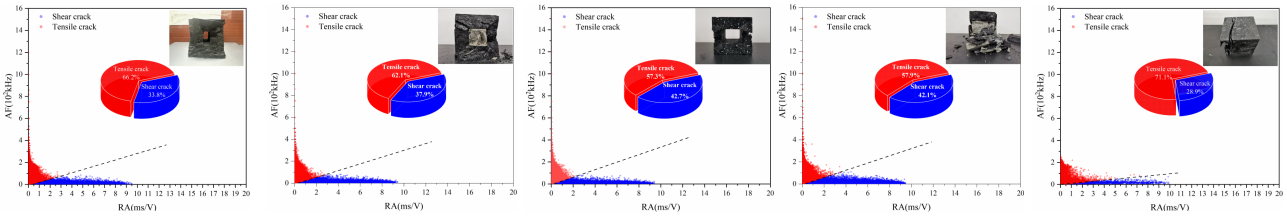

(a) U-C-20 **(b)** B-C-20 **(c)** U-C-60 **(d)** B-C-60 **(e)** U-C-0

Figure 5. RA-AF scatter plot of U-C and B-C specimens.

From the proportion of crack distribution in Figure 5, it can be found that the proportion of tensile cracks in both U-C and B-C specimens identified by AE parameters is greater than that of shear cracks under uniaxial compression. The tensile crack ratio of U-C-0 is 71.1%, occupying a dominant position. With the increase in excavation–backfill width, the proportion of tensile cracks gradually decreases, while the proportion of shear cracks gradually increases. Especially for U-C-60, the proportion of shear cracks is 42.7%, and the shear–tensile ratio is 0.74. The proportion of tensile cracks in the B-C group is generally lower and shows a slow downward trend, decreasing from 66.7% for B-C-20 to 58.3% for B-C-60. In summary, with the increase in excavation–backfill width, the failure mode of specimen transitions from tensile failure to tensile–shear failure, and the crack evolution characteristics of the U-C group are similar to those of the B-C group.

To clarify the process and mechanism of compressive load-induced failure of coal pillars before and after backfill, the full process of compressive failure of U-C and B-C specimens is recorded by the DIC image acquisition system (Figure 6), along with the extract maximum Von-Mises strain and crack initiation strain for all specimens (Table 4). The failure characteristics of U-C and B-C specimens under different excavation–backfill widths are summarized.

As shown in Figure 6, for U-C-0, at the initial loading stage ($0.2\sigma_{peak}$), micro-cracks along the bedding direction appear on the specimen surface under axial loading. With the increase in axial loading ($0.4\sigma_{peak}$–$0.95\sigma_{peak}$), crack evolution on the left side of the specimen is obvious, and significant splitting failure occurs on the right side. When the load reaches the peak (σ_{peak}), extensive splitting occurs along the bedding plane on the right side of the specimen. When the excavation width is 20 mm, at the initial loading stage ($0.2\sigma_{peak}$), the specimen exhibits compressive deformation at the top under axial loading without obvious damage. With the increase in axial loading ($0.4\sigma_{peak}$–$0.95\sigma_{peak}$), transverse cracks appear at the lateral coal wall positions of the specimen, and their number and intensity gradually increase. When the load reaches the peak (σ_{peak}), large longitudinal macrocracks appear at the top coal wall of the specimen. When the excavation width is 60 mm, at the initial stage ($0.2\sigma_{peak}$), vertical cracks appear on the upper and lower surfaces of the rectangular roadway. With the increase in loading intensity ($0.4\sigma_{peak}$–$0.95\sigma_{peak}$), the number of vertical cracks on the upper and lower coal walls increases. When the peak strength (σ_{peak}) is reached, transverse cracks appear on both sides of the coal wall accompanied by partial coal spalling.

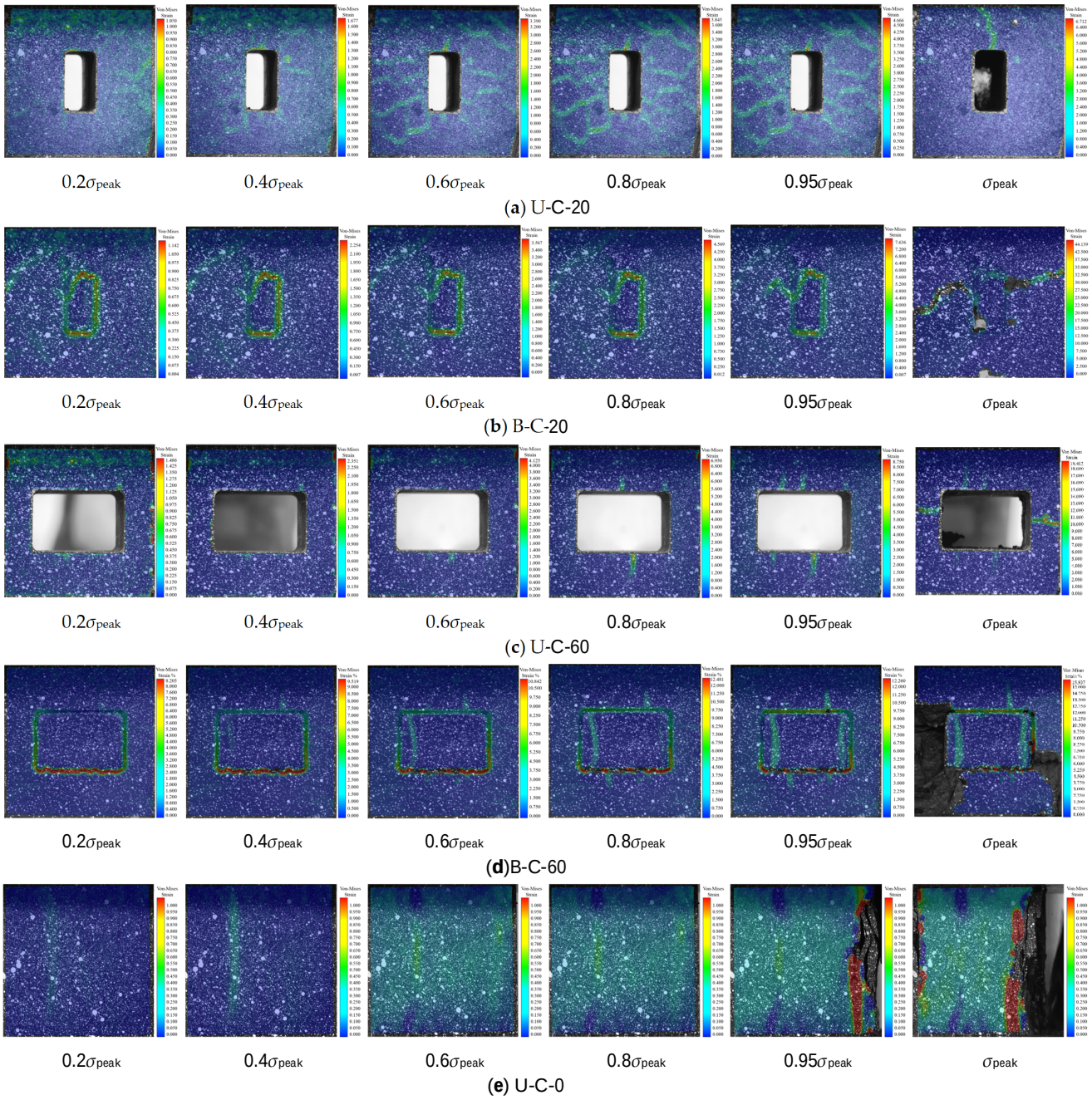

Figure 6. Full-field strain diagram of U-C and B-C specimens.

Table 4. Quantitative strain data of DIC full-field strain maps for U-C and B-C specimens.

Items	$0.2\sigma_{peak}$ Max Strain (%)	$0.4\sigma_{peak}$ Max Strain (%)	$0.6\sigma_{peak}$ Max Strain (%)	$0.8\sigma_{peak}$ Max Strain (%)	$0.95\sigma_{peak}$ Max Strain (%)	σ_{peak} Max Strain (%)	Crack Initiation Strain (%)
U-C-0	0.98 ± 0.05	0.99 ± 0.04	1.00 ± 0.03	1.02 ± 0.06	1.24 ± 0.07	1.65 ± 0.08	1.01 ± 0.04
U-C-20	1.47 ± 0.06	1.82 ± 0.08	2.75 ± 0.10	3.35 ± 0.12	4.67 ± 0.15	6.71 ± 0.18	2.78 ± 0.09
U-C-60	1.49 ± 0.07	2.35 ± 0.09	4.10 ± 0.11	6.95 ± 0.14	8.75 ± 0.16	18.41 ± 0.22	4.15 ± 0.10
B-C-20	1.42 ± 0.06	2.25 ± 0.08	3.57 ± 0.11	4.57 ± 0.13	7.06 ± 0.15	42.50 ± 0.25	3.60 ± 0.10
B-C-60	8.21 ± 0.12	9.52 ± 0.14	10.85 ± 0.15	12.18 ± 0.16	12.26 ± 0.17	15.94 ± 0.19	10.90 ± 0.14

Note: The crack initiation strain is the critical strain when the first macro-crack appears on the specimen surface.

For the B-C specimen, deformation first occurs at the weak interface between the backfill and the coal wall for specimens with different excavation–backfill widths. With

the increase in load, cracks initiate from the weak interface of the backfill and gradually propagate toward the coal wall until coalescence. For the specimen with an excavation–backfill width of 20 mm, cracks initiate from the left weak interface when the load reaches $0.95\sigma_{peak}$ and begin to expand leftward, and the cracks coalesce after the peak stress σ_{peak} is reached. With the increase in excavation–backfill width, the overall damage degree of the specimen during loading intensifies, and vertical cracks are initiated in the backfill.

4. Discussion

4.1. Analysis of AE Fracture Source Locations

Digital image correlation provides the surface strain field, while AE signals reveal the initiation and coalescence of internal micro-cracks. The RA-AF method distinguishes crack types by calculating the ratio of RA to AF for each AE signal. However, a single AE source location is usually inverted from multiple AE signals, and redundant data may lead to deviations in judgment results. Therefore, it is necessary to confirm the fracture type of the AE source location by comparing the fracture types inverted from different AE signals. Figure 7 shows the distribution of AE fracture sources of U-C and B-C specimens [29]. In Figure 7, blue and red dots represent shear and tensile AE fracture sources, respectively, and the size of the dots indicates the magnitude of the fracture source. The statistics of AE fracture sources at each stage are presented in Table 5.

As can be seen from Figure 7, fracture sources are generated mainly in stage II, where micro-cracks nucleate and evolve into macro-cracks. For the U-C-0 specimen (Figure 7e), AE fracture sources are mainly concentrated in the middle bedding plane under uniaxial compression. The number of shear and tensile fracture sources is nearly equal, especially in stage II, with a ratio close to 1, indicating that shear and tensile cracks are almost equivalent and the fracture is relatively balanced. This is because the bedding plane undergoes tensile failure followed by shear slip under compressive stress. When the excavation–backfill width is 20 mm (Figure 7a), the number of tensile fracture sources surges in stage II, accounting for 54.1%, indicating that tensile cracks dominate the specimen, with a significant gap between the number of shear and tensile fracture sources. For the U-C-60 specimen (Figure 7c), AE fracture sources are relatively scattered under uniaxial compression, suggesting the existence of multiple crack propagation paths. The proportion of shear fracture sources is slightly higher than that of tensile fracture sources. With the excavation–backfill width increasing from 0 mm to 60 mm, the failure mode of the specimens gradually transitions from tensile failure to shear failure.

After backfill, the distribution of fracture sources becomes partially scattered across the entire specimen, indicating that the backfill alleviates the concentrated failure caused by stress concentration. For the B-C-20 specimen (Figure 7b), AE fracture sources are mainly concentrated in the middle, with significant tensile fracture sources in stages I and II and a shear–tensile ratio of 0.72, meaning tensile cracks are relatively dominant. This indicates that partial backfill replacement has a minor impact on the physical and mechanical properties of the coal. For the B-C-60 specimen (Figure 7d), fracture sources are more scattered with a shear–tensile ratio of 0.97, which is 0.11 lower than that of the U-C. The incorporation of the backfill transforms the tensile failure cracks in the coal wall into tensile–shear cracks inside the backfill, reducing the risk of coal wall spalling.

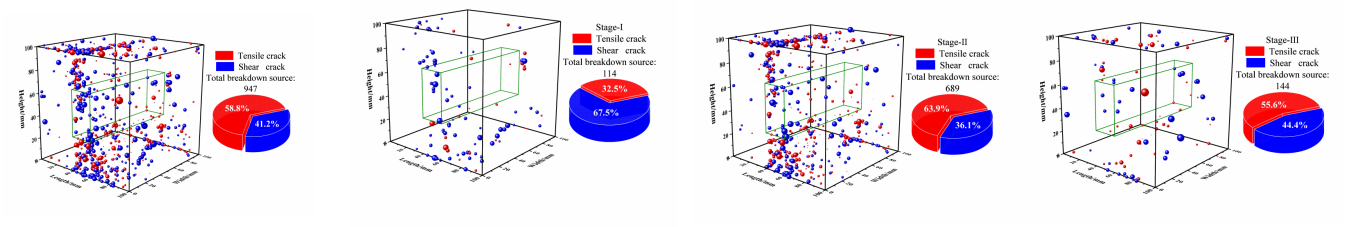

(**a**) U-C-20

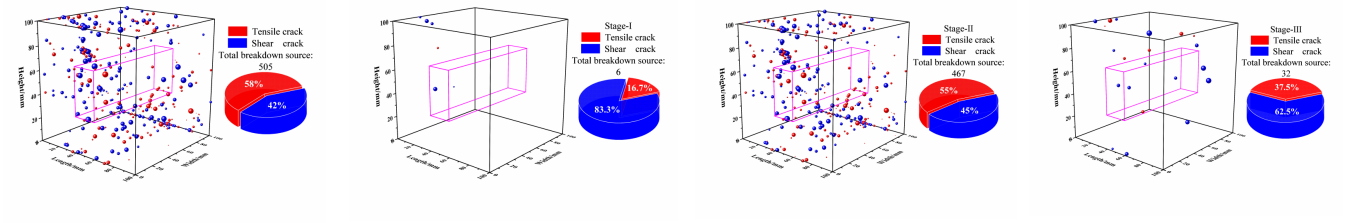

(**b**) B-C-20

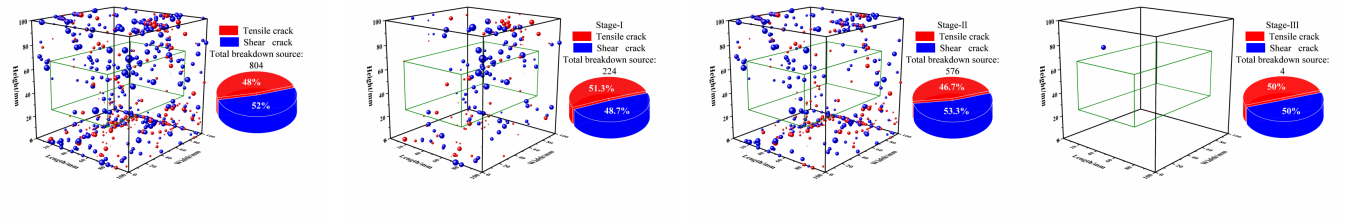

(**c**) U-C-60

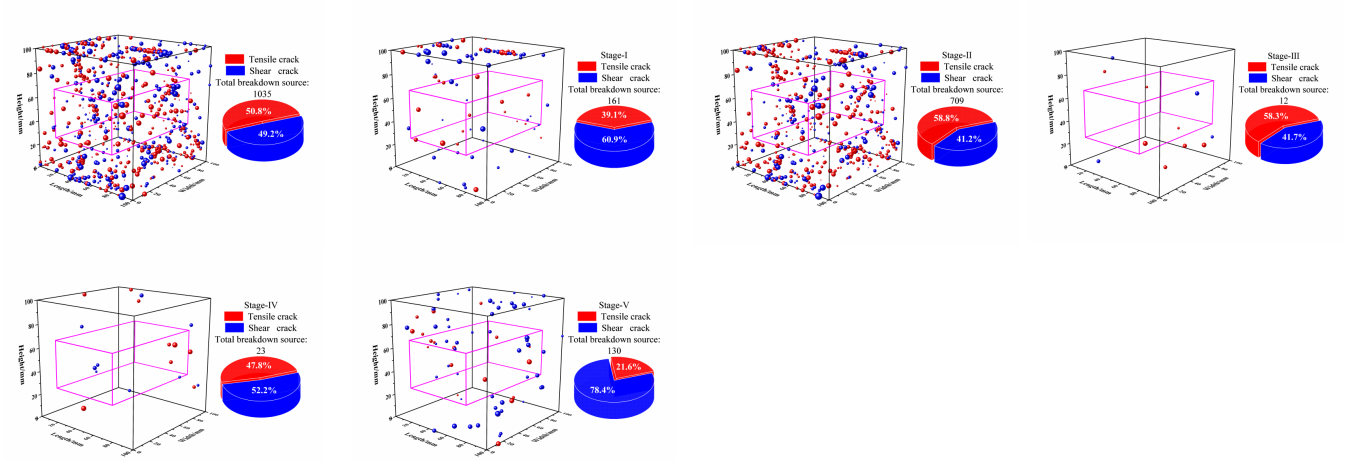

(**d**) B-C-60

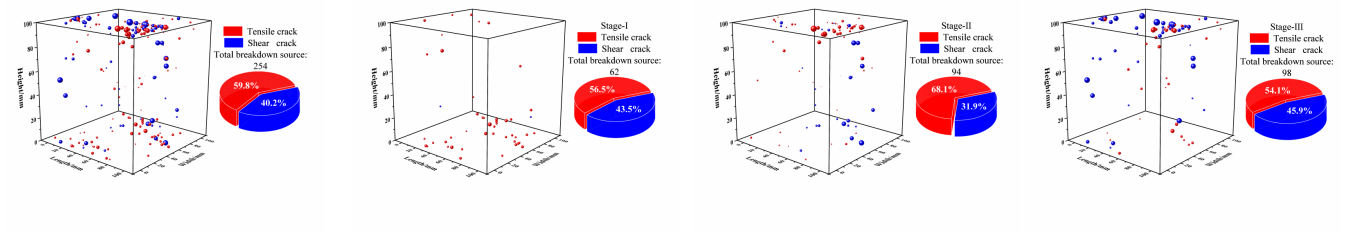

(**e**) U-C-0

Figure 7. AE fracture sources of U-C and B-C specimens.

Table 5. Statistics on acoustic emission fracture sources of specimens.

Items	Shear Fracture Source				Tensile Fracture Source				Proportion	Total Number of Fracture Source
	I	II	III	IV	I	II	III	IV		
U-C-0	27	45	30		35	53	64		0.67	254
U-C-20	77	249	64		37	440	80		0.54	947
U-C-60	109	306	2		115	270	2		1.08	804
B-C-20	212	210	20		293	257	12		0.72	505
B-C-60	98	292	5	112	63	417	7	39	0.97	1035

4.2. Analysis of Crack Chain Evolution

The analysis of AE fracture sources mainly reflects the shear–tensile ratio of failure mode, but it cannot form a macro-failure surface. It judges the failure interface and relative failure mode, and cannot intuitively reflect the rock failure path and crack type. Clustering, a commonly used machine learning method, is usually employed to invert crack failure types. The Single-linkage Cluster (SLC) method [30,31] forms crack evolution links by connecting the closest fracture sources and divides the crack chain evolution links into different sub-clusters based on similarity characteristics, consistent with the crack propagation in local areas of rock [32,33]. In Figure 8, the line segments represent the crack evolution links between different fracture sources, the blue circles indicate the nucleation energy of fracture sources, and different line colors represent the relative average energy of crack evolution.

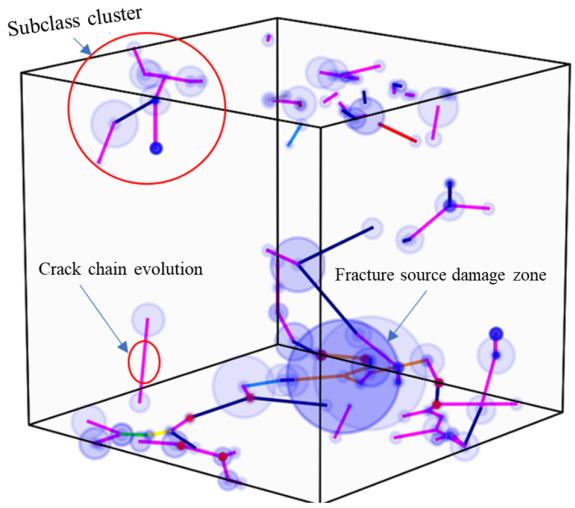

Figure 8. 3D crack chain evolution diagram.

Based on the spatial distance between two AE events, matrix A is constructed, where the element a_{ij} in the i-th row and j-th column corresponds to the spatial distance between the i-th and j-th AE events. The equation (Equation (3)) is expressed as follows:

$$a_{ij} = \sqrt{(x_i + x_j)^2 + (y_i + y_j)^2 + (z_i + z_j)^2} \quad (3)$$

where a_{ij} is the spatial distance between two AE fracture sources; x, y, z are the 3D coordinates of the AE fracture sources.

In SLC hierarchical clustering, the distance between two clusters is defined as the shortest distance between two points belonging to each cluster, linked by feature keys, and there may be M ($0 < M < N/2$) subsets. Based on these subsets, a new distance matrix B is

established, where the element B_{nm} in the n-th row and m-th column represents the spatial distance between subset n and subset m, expressed as (Equation (4)):

$$\begin{cases} B_{nm} = a_{uv} \\ a_{uv} = \min(dist(u,v))(u \in n, v \in m) \end{cases} \quad (4)$$

where n and m are clusters.

Based on Equations (3) and (4), the number of clusters at a certain spatial scale is obtained by setting a similarity threshold or distance threshold during the SLC clustering.

The cluster distribution at different spatial scales can reflect the internal micro-crack propagation, and coalescence of U-C and B-C specimens, as well as the micro–meso–macro-evolution of cracks. A distance threshold of 5 mm is determined as the optimal parameter for SLC clustering, whose selection is based on the geometric size of the cubic specimens (100 × 100 × 100 mm) and the spatial positioning accuracy of the AE system (six sensors with a 40 dB noise threshold). Table 6 shows the subset chain evolution of specimens at different stages. To clarify the crack chain evolution, the visualization range of the fracture source energy circle is reduced through the normalization principle.

Table 6. Crack chain evolution subset link of U-C/B-C specimens.

Items	Stage I	Stage II	Stage III	Items	Stage I	Stage II	Stage III	Stage IV
U-C-20	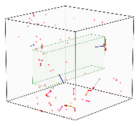	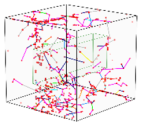	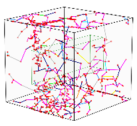	B-C-20	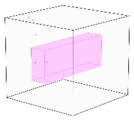	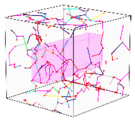	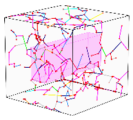	-
U-C-60	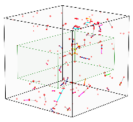	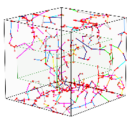	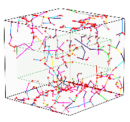	B-C-60	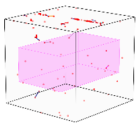	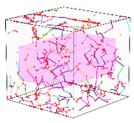	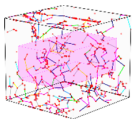	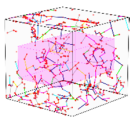
U-C-0	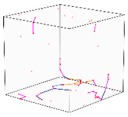	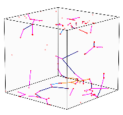	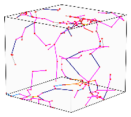					
Legend:	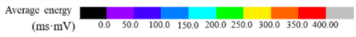							

Table 6 presents the crack chain evolution paths of U-C and B-C based on AE fracture sources. In the compaction stage, there is little crack chain and scattered AE energy, mainly involving the propagation and coalescence of micro-cracks. In the elastic stage, some micro-cracks coalesce, leading to obvious propagation of crack chain. Especially in U-C-0 and U-C-20, cracks propagate along the bedding plane, while in U-C-60, cracks are mainly concentrated at the coal wall, showing tensile–shear mixed cracks. For B-C specimens, parallel cracks are initiated on the bedding plane, and oblique shear cracks are mostly found in the backfill, showing shear failure. Compared with fracture source analysis, this crack chain evolution can better reflect the propagation of macro-cracks. In the yield stage, the crack chain connects to macro-failure cracks, and the specimen is about to lose stability. In the post-peak residual stage, local instability of some specimens leads to the detachment of AE probes, and only the crack evolution of B-C-60 is observed. With the increase in load, the number of cracks increases significantly, and the shear slip of particles inside the backfill allows the structure to gradually release energy, avoiding instantaneous failure.

The crack chains of U-C specimens in stage I are similar to those in stages II and III, so they can be used as precursor directional features for the evolution of macro-failure surface

types and directions to predict the failure path in advance. For B-C specimens, due to the influence of the backfill, the stress concentration along the bedding direction is reduced, resulting in fewer and scattered micro-cracks. However, the crack links of B-C-60 in stage I are similar to those at complete failure, so crack chain evolution can still be used as a precursor feature of the failure mode of B-C specimens. For some specimens, the crack chain in stage II can be selected to predict the failure path, direction, and type.

The crack chain evolution can intuitively judge the failure process of U-C/B-C specimens. The number and orientation of cracks are the key factors determining the failure mode of specimens. The number and orientation of cracks are counted and plotted in Figure 9, where the radial direction represents the number of cracks and the circumferential direction represents the crack direction. As shown in Figure 9, the cracks in the U-C group are mainly distributed in directions nearly parallel to the coal bedding plane (75°~90°, 255°~270°) and nearly perpendicular to the bedding plane (165°~180°). For B-C-60 (Figure 9d), cracks are evenly distributed in all directions, which is consistent with the fracture source location. The presence of the backfill homogenizes the crack chain evolution of the composite and reduces the tendency of crack evolution at the coal wall, but overall, cracks are nearly perpendicular to the bedding direction (165°~180°). To further analyze the crack types in each direction, the number of various cracks is calculated and statistically analyzed by region, as shown in Table 7.

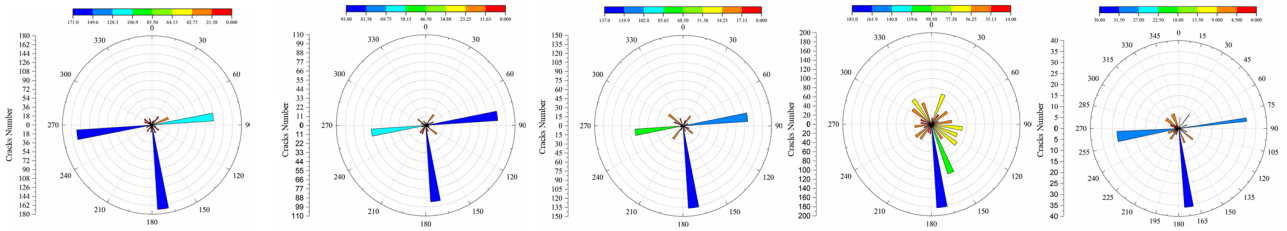

(**a**) U-C-20 (**b**) B-C-20 (**c**) U-C-60 (**d**) B-C-60 (**e**) U-C-0

Figure 9. Crack orientation and quantity distribution diagram of U-C and B-C specimens.

Table 7. Crack type statistics of U-C and B-C specimens.

Items	(C_c) [0°~15°]	(C_{cs}) (15°~30°]	(C_{as}) (30°~60°]	(C_t) (60°~90°]	Total Number
U-C-0	3	7	38	128	176
U-C-20	622	172	126	132	1052
U-C-60	11	35	133	346	525
B-C-20	9	23	125	205	375
B-C-60	168	496	384	108	1156

As can be seen from Table 7, the number of compressive cracks (C_c) in both U-C and B-C groups is relatively low. However, the number of C_c in U-C-20 is 622, much higher than other cracks, which may be caused by the existence of micro-cracks in the coal, as evidenced by the micro-strain analysis in the compaction and elastic stages in Figure 9a. In addition, the number of C_c in B-C-60 is relatively high (168), mainly due to the uneven stress transfer between the backfill and the coal, as well as the initial transverse cracks caused by incomplete backfill, which increases the number of C_c. The number of C_c in the B-C group is higher than that in the U-C group. Combined with the stress phenomenon in DIC images, it can be explained that the interface leads to an increase in C_c, which may affect the stability of the specimens. The number of compression–shear cracks (C_{as}) in the B-C group is significantly higher than that in the U-C group, especially in U-C-20. In U-C-20, transverse cracks are initiated along the bedding plane, leading to tensile stress

and cracking of the bedding plane. Tensile cracks (C_t) mainly appear in the U-C group, especially in U-C-0, where the proportion of C_t reaches 72.73%.

The shear–tensile ratios of different specimens are calculated: 0.739, 0.307, and 0.673 for the U-C group, and 0.581 and 0.109 for the B-C group. The calculation results exclude the influence of compressive cracks on the shear–tensile ratio, and the dominant failure trend is consistent with the results of RA-AF and AE fracture source analysis. Therefore, it can be used as an intuitive method to further distinguish the failure mode.

4.3. Limitations and Prospects

We acknowledge the limitation that the experiments are conducted under uniaxial compression, while field coal pillars are subjected to triaxial stress. The choice of uniaxial testing is to first clarify the fundamental mechanical bearing characteristics and crack evolution mechanism of the coal pillar "excavation-backfill" composite, eliminating the interference of confining pressure to isolate the core effect of backfill and interface behavior—this provides a critical baseline for subsequent triaxial studies. We emphasize that the results should be generalized cautiously to field conditions, where confining pressure may enhance the composite's strength and alter crack propagation paths.

We propose to (1) optimize the backfill recipe for different excavation widths, especially prioritizing this ratio for 60 mm width to maximize strength recovery; (2) enhance coal wall surface roughness before backfilling to improve interfacial bonding; and (3) incorporate the uniaxial test-derived crack evolution laws into numerical simulations for field pillar design.

5. Conclusions

The mechanical response of unfilled coal pillar (U-C) and backfill coal pillar (B-C) is divided into four stages: pore compaction, elastic, yield, and post-peak residual. For unfilled coal pillars (U-C), increasing the excavation–backfill width from 20 mm to 60 mm reduces compressive strength by 30.07% and 64.88%. In contrast, B-C specimens show a remarkable strength recovery—with a decrease of 43.36% (B-C-60), and the 60 mm width identified as the critical value for optimal backfill efficiency.

Based on the analysis of temporal characteristics of acoustic emission (AE), both the U-C and B-C groups exhibit a four-stage AE evolution law under uniaxial compression: quiet period, rising period, active period, and post-peak rising period. The post-peak rising period is mainly observed in the B-C group, indicating that the backfill distinctly alters the mechanical behavior of coal samples. The *b*-value fluctuates upward during the pore compaction and elastic stages with energy release, decreases significantly during the yield stage with substantial energy release, and shows an increased fluctuation amplitude during the post-peak stage due to enhanced crack propagation and frictional slip. The RA-AF values reveal that the failure mode of both groups transitions from tensile failure to tensile–shear failure with the increase in excavation–backfill width, which is also verified by digital image correlation observations.

3D crack chain evolution is inverted based on the temporal characteristics of AE source locations. The cracks in the U-C group are mainly distributed along the coal bedding direction (75°~90°, 255°~270°) and vertical direction (165°~180°), while those in the B-C are more uniformly distributed. This demonstrates that the backfill distinctly influences crack distribution, with cracks predominantly appearing nearly perpendicular to the bedding direction (165°~180°).

Engineering-wise, these results guide field practice: adopting the gangue-based cemented paste backfill (cement: fly ash: gangue powder: water = 1:1:3:1.83) for 60 mm wide excavations maximizes coal resource recovery while enhancing composite stability, provid-

ing a reliable technical basis for the "excavation-backfill-retention" mining technology's safe application.

Author Contributions: H.S.: Conceptualization, Resources, Supervision, Funding Acquisition; J.Z. (Jingmin Zhang): Conceptualization, Formal Analysis, Writing—Original Draft, Writing—Review and Editing; X.M.: Data Curation, Validation; J.Z. (Jin Zhang): Conceptualization, Methodology, Supervision. All authors have read and agreed to the published version of the manuscript.

Funding: This research was supported by the National Natural Science Foundation of China (No. 52574272); Shaanxi Provincial Natural Science Foundation (2025JC-YBMS-369).

Data Availability Statement: All data referenced in this paper will be made available upon request.

Conflicts of Interest: The authors declare that there are no conflicts of interest regarding the publication of this paper.

References

1. Wang, S.; Liu, L.; Zhu, M.; Wei, B.; Zhuang, D.; Qu, H.; He, W.; Shao, C.; Xia, L.; Zhou, J. Scientific problems and technology of the integration of "excavation-backfill retention" of section coal pillar and mining roadway. *J. China Coal Soc.* **2024**, *49*, 3291–3315.
2. Wang, J.; Yan, C. Influence of district coal pillars recovery on wall rock instability in gob-side entry retaining and the control measures. *Coal Eng.* **2024**, *56*, 38–45.
3. Qiao, Y.; Meng, Z.; Zhu, S.; Chen, J.; Liu, L.; Zhang, Y. Study on coal pillar failure mechanism and surrounding rock control technology under influence of secondary mining. *Coal Sci. Technol.* **2020**, *48*, 71–77.
4. Xie, Z.; Qiu, S.; Li, S.; Jiang, Q.; Xu, D.; Zheng, M. Excavation damage mechanism of deep buried layered fractured rock mass based on three-dimensional bonded block damage model. *Comput. Geotech.* **2025**, *180*, 107101. [CrossRef]
5. Sayadi, S.; Baghbanan, A.; Delgado-Martín, J. Experimental investigation of fracturing processes under compression of granite specimens containing combined defects using DIC and AE techniques. *Rock Mech. Rock Eng.* **2025**, *59*, 1483–1506. [CrossRef]
6. Wang, L.; Xue, Y.; Zhu, L.; Cao, X.; Li, X.; Ranjith, P.G. Fracture evolution of granite under cyclic thermal shocks: Effects of liquid nitrogen cooling on strength, toughness, and acoustic emission characteristics. *Therm. Sci. Eng. Prog.* **2026**, *70*, 104507. [CrossRef]
7. Jing, H.; Wu, J.; Yin, Q.; Meng, B.; Zou, F. Experimental study on multi-source information response of force electromagnetic and acoustics in the whole process of deformation and fracture evolution of structural surrounding rock. *Chin. J. Rock Mech. Eng.* **2023**, *42*, 1582–1598.
8. Jiang, Q.; Liu, Q. Mechanical similarity distortion mapping principle and case analysis for underground cavern physical simulation of deformation and failure. *Rock Soil Mech.* **2024**, *45*, 20–37.
9. Hou, G.; Liang, J.; Jing, H.; Hu, T.; Tan, J.; Yang, X.; Zhang, Y. Acoustic emission characteristics of thick-walled cylinder specimen subjected to triaxial loading during excavation unloading. *Rock Soil Mech.* **2019**, *40*, 4564–4572.
10. Wang, Y.; Zhu, L.; Xue, Y. A Comprehensive review on dual-pathway utilization of coal gangue concrete: Aggregate substitution, cementitious activity activation, and performance optimization. *Buildings* **2026**, *16*, 302. [CrossRef]
11. Chang, X.; Wu, S.; Cheng, H.; Dai, F.; Zhang, Z. Experimental study and acoustic emission frequency domain analysis of spalling-rockburst in high-stress tunnel surrounding rock. *J. Min. Strat. Control Eng.* **2024**, *6*, 101–114.
12. Xin, J.; Jiang, Q.; Gong, F.; Liu, L.; Liu, C.; Liu, Q.; Yang, Y.; Chen, P. Mechanical behaviors of backfill-rock composites: Physical shear test and back-analysis. *J. Rock Mech. Geotech. Eng.* **2024**, *16*, 807–827. [CrossRef]
13. Xin, J.; Jiang, Q.; Zhai, D.; Feng, G.L.; He, B.G.; Li, S.J. Shear-induced rockburst of double-tunnel rocks subjected to shear loading: A comparative analysis. *J. Cent. South Univ.* **2023**, *30*, 4207–4229. [CrossRef]
14. Zhu, Q.; Ma, C.; Li, X.; Li, D. Effect of filling on failure characteristics of diorite with double rectangular holes under coupled static-dynamic loads. *Rock Mech. Rock Eng.* **2021**, *54*, 2741–2761. [CrossRef]
15. Lee, J.W.; Park, E.S.; Choi, J.; Oh, T.M.; Kim, M.J. Acoustic emission characteristics during damage-zone formation around a circular opening. *Geomech. Eng.* **2024**, *36*, 511.
16. Zhu, Q.Q.; Li, D.Y.; Li, X.B. Experimental study on failure and mechanical characteristics of marble containing a prefabricated elliptical hole. *Chin. J. Rock Mech. Eng.* **2019**, *38*, 2724–2733.
17. Liu, G.; Wang, S.; Wang, D.; Yang, Z.; Zan, Y. Deformation damage and acoustic characteristics behind sandstone under different shapes of tunnels by cyclic loading. *J. Heilongjing Univ. Sci. Technol.* **2024**, *34*, 839–846.
18. Wu, H.; Zhao, G.; Liang, W. Mechanical properties and fracture characteristics of pre-holed rocks subjected to uniaxial loading: A comparative analysis of five hole shapes. *Theor. Appl. Fract. Mech.* **2020**, *105*, 102433. [CrossRef]
19. Gong, F.; Wu, W.; Li, T.; Si, X. Experimental simulation and investigation of spalling failure of rectangular tunnel under different three-dimensional stress states. *Int. J. Rock Mech. Min. Sci.* **2019**, *122*, 104081. [CrossRef]

20. Wu, H.; Zhao, G.; Liang, W. Investigation of cracking behavior and mechanism of sandstone specimens with a hole under compression. *Int. J. Mech. Sci.* **2019**, *163*, 105084. [CrossRef]
21. Zhou, Z.; Tan, L.; Cao, W.; Zhou, Z.; Cai, X. Fracture evolution and failure behavior of marble specimens containing rectangular cavities under uniaxial loading. *Eng. Fract. Mech.* **2017**, *184*, 183–201. [CrossRef]
22. Xiang, J.; Zhao, C.; Liu, Q.; Zhao, Y.; Guo, Y.; Fei, X. Mechanism of bio-carbonation on leaching behavior: A case study of coal gasification slag-based binder. *Constr. Build. Mater.* **2026**, *513*, 145441. [CrossRef]
23. Cheng, A.; Shu, P.; Zhang, Y.; Wang, P.; Wang, M.X. Acoustic emission characteristics and damage constitution of backfill-surrounding rock combination. *J. Min. Saf. Eng.* **2020**, *37*, 1238–1245.
24. Li, S.; Lu, Y.; Liu, J. The Study of Sample Size on b-value Statistics in the Gutenberg-Richter's Law. *Technol. Earthq. Disaster Prev.* **2018**, *13*, 636–645.
25. Zhang, L.M.; Ma, S.Q.; Ren, M.Y.; Jiang, S.Q.; Wang, Z.Q.; Wang, J.L. Acoustic emission frequency and b value characteristics in rock failure process under various confining pressures. *Chin. J. Rock Mech. Eng.* **2015**, *34*, 2057–2063.
26. Liu, X.L.; Liu, Z.; Li, X.B.; Han, M.S. Acoustic emission b-values of limestone under uniaxial compression and Brazilian split ting loads. *Rock Soil Mech.* **2019**, *40*, 267–274. (In Chinese)
27. Rao, M.V.M.S.; Lakshmi, K.P. Analysis of b-value and improved b-value of acoustic emissions accompanying rock fracture. *Curr. Sci.* **2005**, *89*, 1577–1582.
28. Liu, C.; Jiang, Q.; Xin, J.; Wu, S.; Liu, J.; Gong, F. Shearing damage evolution of natural rock joints with different wall strengths. *Rock Mech. Rock Eng.* **2022**, *55*, 1599–1617. [CrossRef]
29. Bi, J.; Zhao, Y.; Wu, Z.; Li, J.; Wang, C. Research on crack classification method and failure precursor index based on RA-AF value of brittle rock. *Theor. Appl. Fract. Mech.* **2024**, *129*, 104179. [CrossRef]
30. Zhang, Z.; Wang, E.; Li, N. Fractal characteristics of acoustic emission events based on single-link cluster method during uniaxial loading of rock. *Chaos Solit. Fractals* **2017**, *104*, 298–306. [CrossRef]
31. Zhou, J. Concrete Crack Detection Method and Application Based on Hierarchical Clustering. Master's Thesis, Beijing University of Chemical Technology, Beijing, China, 2021.
32. Zhang, Y.; Zhang, S.; Deng, Z.; Wang, R.; Liu, G. A prediction method for coalbed methane development sweet spots based on hierarchical analysis and grey fixed-weight clustering: Taking Shizhuangbei block as an example. *Coal Sci. Technol.* **2024**, *52*, 166–175.
33. Liu, J.; Li, Y.; Tian, J.; Zhao, X.; Liu, H.; Gan, H. Experimental study of temporal and spatial distribution characteristics of acoustic emission during rock fracture based on single-link cluster method. *Chin. J. Rock Mech. Eng.* **2010**, *29*, 3488–3497.

Disclaimer/Publisher's Note: The statements, opinions and data contained in all publications are solely those of the individual author(s) and contributor(s) and not of MDPI and/or the editor(s). MDPI and/or the editor(s) disclaim responsibility for any injury to people or property resulting from any ideas, methods, instructions or products referred to in the content.